Journal of Applied Physics ARTICLE pubs.aip.org/aip/jap

Flexible metasurfaces as sub-6 GHz frequency selective surfaces for 5G applications

Cite as: J. Appl. Phys. **134**, 145304 (2023); doi: 10.1063/5.0167167
Submitted: 10 July 2023 · Accepted: 23 September 2023 ·
Published Online: 11 October 2023

E. M. Materón,[1,2] H. R. D. Filgueiras,[3] E. C. Vilas Boas,[4] F. R. Gómez,[5] F. R. P. Cavalcanti,[5] Y. C. B. Silva,[5] Arismar Cerqueira S., Jr.,[4] F. A. P. de Figueiredo,[4] L. L. Mendes,[4] Osvaldo N. Oliveira, Jr.,[1] and J. R. Mejía-Salazar[4,a)]

AFFILIATIONS

[1]Sao Carlos Institute of Physics, University of Sao Paulo, P.O. Box 369, 13560-970 Sao Carlos, SP, Brazil
[2]Sao Carlos Institute of Chemistry, University of Sao Paulo, 13566-590 Sao Carlos, SP, Brazil
[3]5G Innovation Office, VS Telecom, 04213-001, Sao Paulo, SP, Brazil
[4]National Institute of Telecommunications (Inatel), 37540-000 Santa Rita do Sapucaí, MG, Brazil
[5]Teleinformatics Engineering, Federal University of Ceará, Fortaleza, Brazil

[a)]**Author to whom correspondence should be addressed:** jrmejia3146@gmail.com

ABSTRACT

The deployment of fifth-generation mobile network (5G), beyond 5G and sixth-generation mobile network platforms encounters challenges of blockage, interference, and path loss in radio mobile environments. Metasurfaces provide a promising solution to address these limitations. In this paper, we present a methodology for developing ultrathin flexible metasurface-based frequency selective surfaces (FSSs). Our approach combines thermal evaporation for metallic thin films with a macroscopic metasurface mask (something analogous to screen-printing but using thermal evaporation instead of inks). As a proof of concept, we fabricate a sub-6 GHz metasurface-based FSS using gold deposition on a flexible polyethylene terephthalate substrate. Experimental results are validated through numerical full-wave simulations using COMSOL Multiphysics and equivalent-circuit model simulations. The metasurface operates within the primary frequency band utilized in 5G networks (3–5 GHz), indicating its potential applicability across a wide range of flexible, conformal, and wearable devices. The fabricated FSS can be installed on surfaces of any shape, such as flat or curved windows, as well as on walls or other external surfaces. This methodology offers practical solutions for wireless communications and enhancing signal transmission in diverse environments.

I. INTRODUCTION

The fifth-generation mobile network (5G) has been designed with a flexible architecture to cater to various service requirements. It should manage resources efficiently to support contrasting demands in offering high throughput, massive number of connections, low latency, robustness, and long reach. This flexibility is achieved by mapping services and applications into four primary scenarios:[1–6] extreme mobile broadband (eMBB), massive machine-type communications (mMTC), ultra-reliable low latency communications (URLLC), and enhanced remote area communications (eRAC). The eMBB services may allow for new mobile applications by boosting the data rate experienced by the user.[1,2] Developing mMTC applications will require a large number of devices connected to the mobile network, whose management will be challenging, especially with regard to energy efficiency.[3,4] Latency-sensitive applications require fast response and robustness from the network since retransmission protocols cannot be applied.[5] The URLLC provides the necessary robustness and reduces the overall latency of the radio access network (RAN) to support latency-sensitive applications. Finally, eRAC provides coverage and robustness for applications in rural and remote areas, e.g., in agribusiness, mining industries, border surveillance, and environmental and disaster monitoring.[6] In order to meet so many requirements, two frequency bands are considered for 5G networks.[7] The first one, defined as Frequency Range 1 (FR1), covers the sub-6 GHz bands from 450 MHz up to 6 GHz. The second one, named Frequency Range 2 (FR2), covers the millimeter waves (mm-Waves) from 24.25 up to 52.60 GHz.

FR1 is generally divided into a sub-3 GHz band used for mobile network legacy, providing good coverage but with limited spectrum, and the C-band with channels possessing bandwidth up to 100 MHz. The C-band allows for higher data rates,[8] but it suffers from uplink–downlink imbalance due to the reduced coverage for uplink transmission.[9,10] Sub-3 GHz frequencies are used in the eRAC scenario, urban environments, and as supplementary uplink channels for the C-band solution to the uplink–downlink imbalance. C-band channels are reserved for urban applications to provide basic capacity and coverage. FR2 provides channels with bandwidth up to 400 MHz, allowing a throughput above 1 Gbps. However, at these higher frequencies, the wireless propagation is limited by the severe path loss and blockage.[11,12] With shorter wavelengths, FR2 channels have coverage reduced by attenuation from objects, persons, rain, and atmosphere absorption. The FR2 band is expected to be used in 5G mm-wave self-backhaul in dense urban environments or for small cells in an ultra dense network (UDN) architecture,[13] but the problems associated with limited coverage and path loss need to be tackled.

The challenges of improving wireless signal propagation across various frequencies ranging from microwave to terahertz (THz) have been addressed with novel materials, devices, and strategies. One such strategy involves the use of metasurfaces, which are artificial two-dimensional subwavelength structures, also known as 2D metamaterials.[14,15] Metasurfaces may be used to customize transmission, reflection, and absorption properties of electromagnetic waves.[16–21] The operating frequency of a metasurface is determined by the design of its unit cells, which mimic the behavior of atoms or molecules in a crystal, governing local electromagnetic interactions. These metasurfaces can be used to create devices with diverse electromagnetic functionalities, including absorption control, analog processing, anomalous reflection/refraction, asymmetric reflection, beamforming, beam splitting, collimation, focusing, frequency harmonic conversion, polarization conversion, vortex waves, and spatial filtering. Hence, metasurfaces constitute a core technology for implementing reconfigurable intelligent surfaces (RISs) in 5G applications,[22–24] 6G development,[25,26] and visible light communication (VLC) systems.[27,28] Spatial filtering devices made with metasurfaces are referred to as frequency selective surfaces (FSSs). FSSs consist of thin planar layers of subwavelength structures that interact with electromagnetic waves, enabling selective transmission, reflection, or absorption based on their frequency.[29,30] FSSs meet line-of-sight (LOS) requirements, ensuring uninterrupted wireless signal propagation by mitigating disruptions caused by nearby wireless devices. They provide electromagnetic compatibility and act as shields, while also offering the capability to reflect impinging waves in desired directions to bypass obstacles and enable the implementation of high-gain radiators. Traditionally, FSSs have been manufactured using rigid dielectric slabs, often utilizing printed-circuit-board methods for sub-6 GHz applications.[31] However, these substrates are unsuitable for nonplanar surfaces, which are required in many practical scenarios.[32]

Metasurfaces fabricated using nanomaterials and nanofabrication tools[33] offer the desired characteristics of flexibility, stretchability, and conformability to various surfaces.[34,35] Several methods have been used to produce these metasurfaces, including chemical vapor deposition for graphene and copper etching,[35] inkjet printing,[36] and screen-printing techniques.[37,38] However, conventional inkjet and screen-printing methods have limitations, particularly, in terms of the frequency range and the irregular distribution of metal ink on the surface, which can adversely affect the electromagnetic response of the devices. In this work, we employed screen-printed nanometric films to produce high-quality flexible metasurfaces. Our approach combines a straightforward method for fabricating sample masks with thermal evaporation of thin metal films. This methodology offers several advantages, including high deposition rates, simplicity, and low equipment costs. It eliminates the need for expensive clean rooms, harmful reagents, and printers that require costly additive-rich inks.[39] It also ensures higher reproducibility of the metal film and improved control of parameters compared to conventional inkjet and screen-printing techniques. To demonstrate the feasibility of our methodology, we have developed a sub-6 GHz metasurface functioning as a frequency selective surface (FSS) on a flexible polyethylene terephthalate (PET) substrate.

The paper is organized into four sections. Section II presents the materials and methodology to prototype high-quality metasurface using screen-printed nanometric films. It also discusses the measurement setup used to characterize the fabricated sub-6 GHz metasurface-based FSS. Section III presents the metasurface-based FSS numerical full-wave results and the equivalent circuit model (ECM) simulations. Indeed, the prototype and experimental results are outlined to demonstrate the feasibility of our methodology in applying thermal evaporation for metallic thin films with screen-printing. Finally, conclusions and final comments are included in Sec. IV.

II. MATERIALS AND METHODS

Electromagnetic full-wave simulations were carried out, using the RF module of the commercial software COMSOL Multiphysics, to obtain the corresponding *S*-parameters. The metasurface was considered a periodic 2D infinite array of unit cells (using Floquet periodic boundary conditions) surrounded by air. Numerical reflections were avoided using absorbing perfectly matched layers (PMLs) at the top and bottom of the unit cell. The excitation of the structure was made using electromagnetic plane waves. Then, to demonstrate our fabrication mechanism, we search in the available literature a simple geometry that enables robust polarization stability, i.e., a unit cell design that works in the same way independently of the incident polarization. The most simple example we found was the cross-like design used in this work, which has a perfect mirror symmetry for rotations of 90° on the metasurface's plane.

In the fabrication process, the metasurface mask was built using low-cost materials and an inexpensive cutter printer, with the unit cells designed with AutoCAD software. Silhouette Studio version V3 software was used to make the pattern for the cutter printer. The vinyl adhesive sheet was cut using the cutter printer, and undesired portions were peeled off using tweezers, leaving the designed layout as a negative mask forming a stencil. This stencil was transferred onto a 100 μm thick PET sheet (transparency film for laser printers). Then, 60 nm chromium and 150 nm gold films were deposited by thermal evaporation (using an evaporator

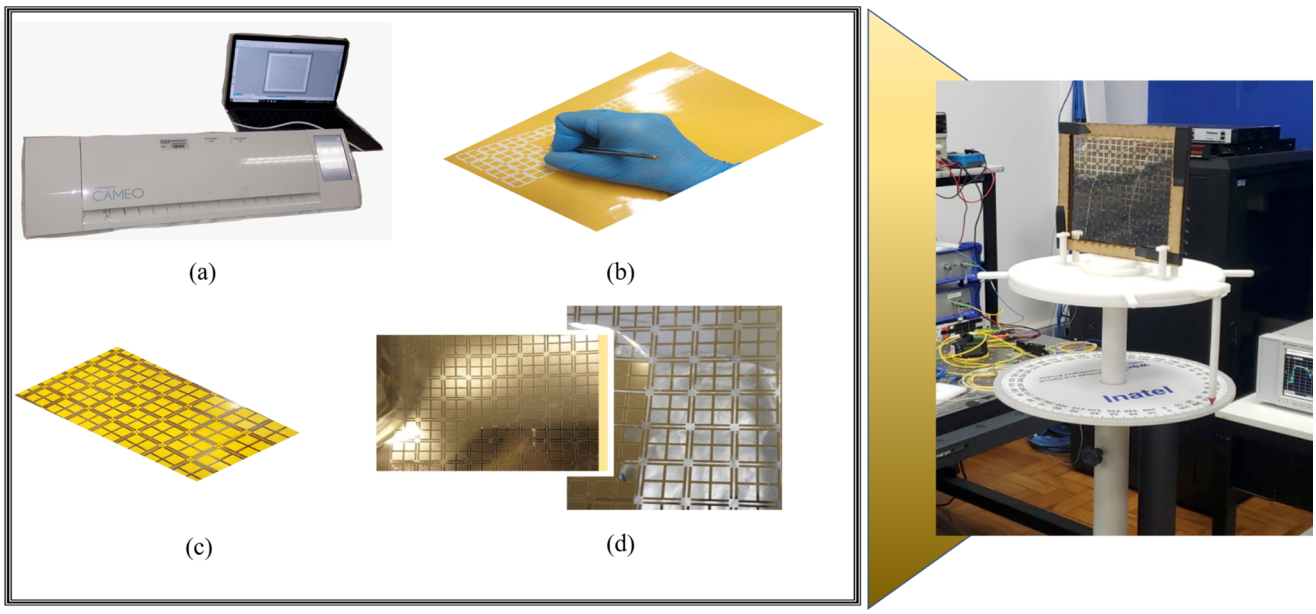

FIG. 1. Design and fabrication of the metasurface. (a) Silhouette Studio version V3 software and cutter printer to prepare the patterns. (b) Undesired portions were peeled off using tweezers and (c) put on a PET sheet. (d) After depositing the nanometric film onto a PET substrate, the mask is removed. The metasurface was prepared for measurements and characterization, as shown in the inset on the right panel.

BALZERS BAK 600) on top of the template with the PET sheet. The vacuum chamber, evacuated by rotary and diffusion pumps, reached a pressure of $\sim 6 \times 10^{-6}$ mbar. The tungsten boat to evaporate gold and chromium had 10 mm in diameter and 0.2 cm^3 volume. The temperature reached for evaporation was 1900 and 1063°C for chromium and gold, respectively. Since the vaporized particles travel from the heating source to collide with the substrate surface (PET polymer), where they condense and adhere to the substrate, forming a thin film, the temperature at the PET polymer was not sufficient to cause any deformation. Hence, the desired pattern was obtained on the substrate, as shown in Figs. 1(a)–1(d), after removing the mask.

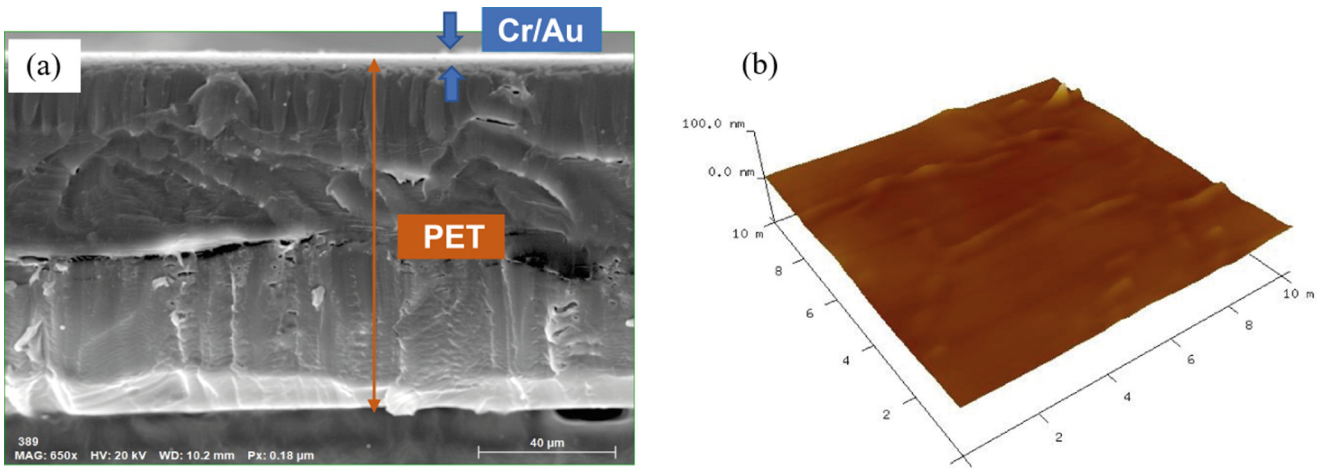

FIG. 2. (a) A cross-section FEG-SEM micrograph of the sample consisting of an adhesive layer of chromium (60 nm) and gold (150 nm), grown on PET by thermal evaporation. (b) AFM image of the thin film surface of gold.

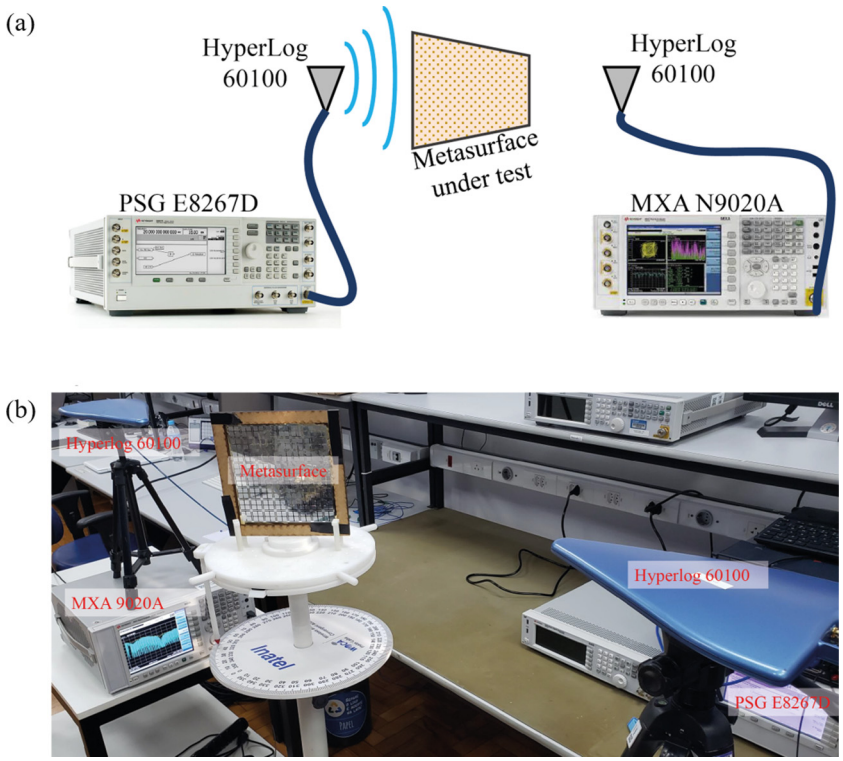

FIG. 3. Experimental setup for characterizing the metasurface. (a) The device under test was placed between two hyperlog antennas. The signal generated by PSG E8267D is analyzed with MXA N9020A. (b) Photograph from the characterization experiment.

Figure 2(a) shows a FEG-SEM image of the metallic nanostructure, comprising a chromium layer (60 nm) followed by a 150 nm thick gold layer on top of the PET substrate. The film smoothness was confirmed with AFM as indicated in Fig. 2(b), featuring a roughness of some tens of nanometers. This level of roughness is negligible compared with the working wavelength of the metasurface and does not affect the electromagnetic properties of the nanostructure.

The metasurface was characterized using two pieces of equipment as depicted in Fig. 3(a): a vector signal generator from Keysight, model PSG E8267D, and a spectrum analyzer model MXA N9020A from the same manufacturer. Two commercial Aaronia Hyperlog 60100 antennas were used for transmitting and receiving the signal from 3 to 5 GHz. The antennas have approximately 5-dBi gain each and bandwidth from 680 MHz to 10 GHz. The distance between the antennas was set as 1.25 m to ensure far-field measurements up to 5 GHz. Figure 3(b) contains a photograph of the setup with the metasurface structure placed above a turn table, with 1°-precision, for enabling characterization with different incident angles. Characterization was performed in two steps

- without the metasurface between the antennas, so the received power would be used as a reference and
- with the metasurface between transmitting and receiving antennas to evaluate the losses caused by the metasurface.

We conducted the measurements by setting a frequency sweep in the PSG vector signal generator, with 2001 points from 3 to 5 GHz. The MXA spectrum analyzer was set in the *maxhold* function with 1001 points so that a continuous line could be observed. The metasurface transmission coefficient (S_{21}) was estimated by computing the difference between the curves from the previous steps.

III. RESULTS AND DISCUSSION

$$G(p, x, \lambda, \theta) = \frac{1}{2}\frac{(1-\beta^2)^2\left[\left(1-\frac{\beta^4}{4}\right)(C_{1+}+C_{1-})+4\beta^2 C_{1+}C_{1-}\right]}{\left(1-\frac{\beta^4}{4}\right)+\beta^2\left(1+\frac{\beta^2}{2}-\frac{\beta^4}{8}\right)(C_{1+}+C_{1-})+2\beta^6 C_{1+}C_{1-}}, \quad (1)$$

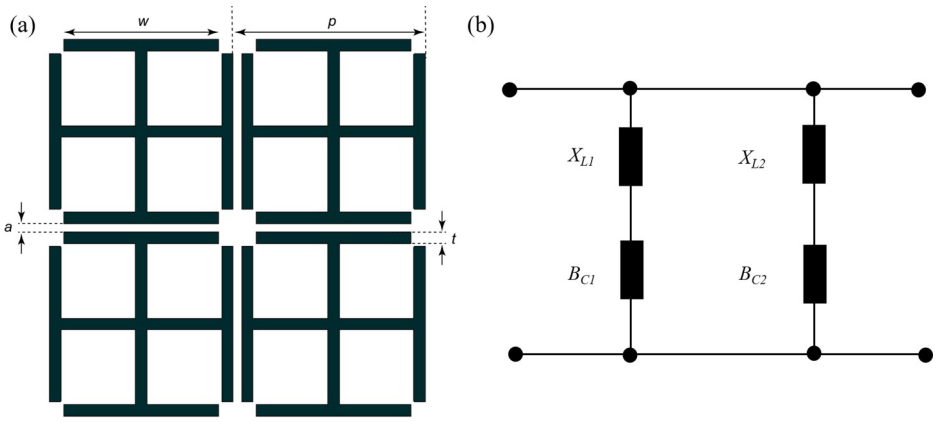

FIG. 4. (a) Schematic representation of a 2 × 2 arrangement of unit cells in the metasurface, (b) the ECM for one cell.

$$\beta = \sin\left(\frac{\pi x}{2p}\right). \tag{2}$$

The feasibility of our concept to fabricate metasurfaces on flexible substrates was proven with a band-stop unit cell following the well-known Jerusalem cross,[40] in an arrangement of 8 × 8 Jerusalem crosses. This geometry has been chosen due to its inherent angular stability and well-known ECM. Flexible metasurfaces are planned to be implemented upon irregular, non-flat, and conformal surfaces that are inevitably subjected to an array of incident angles as the propagating wave interfaces with the surface. Additionally, the efficiency of the manufacturing method is proven by comparing numerical and simulated results with those obtained from experiments, including for oblique incidence.

The corresponding geometrical parameters shown in Fig. 4 are described in Table I, which also presents the final cell dimensions. Each unit cell can be represented by an ECM comprising a parallel combination of two series *LC* circuits, as seen in Fig. 4.[41] The inductive reactance (X_{L1}) and the capacitive susceptance (B_{L1}) define the Jerusalem cross cell first resonance, which is related to the cross-strip lines. The second series *LC* circuit is represented by an inductive reactance (X_{L2}) and a capacitive susceptance (B_{L2}), which is related to the dipole strip lines at the end of each cross arm and resonates at a second frequency higher than the first. Since we are interested in the first resonance to prove the feasibility of the concept of fabricating metasurfaces on flexible substrates, the ECM analysis is restricted to the first arm with transverse electric wave (TE) and transverse magnetic wave (TM)-incidence.

TABLE I. Geometrical parameters and final dimensions of the Jerusalem cross cell unit of the metasurface-based FSS.

Parameter description	Parameter	Value (mm)
Separation between adjacent unit cells	a	0.9403
Width of metallic lines	t	1.253 73
Length of external metallic line	w	16.9254
Array cell period	p	21

The cell dimensions define the inductive reactance and capacitive susceptance and are normalized to the free space characteristic impedance. For TE-incidence, X_{L1} and B_{C1} are, respectively, given by[40–42]

$$X_{L1_{\mathrm{TE}}} = \frac{p}{\lambda}\cos(\theta)[G(p, t, \lambda, \theta) - \ln(\sin(\beta))], \tag{3}$$

$$B_{C1_{\mathrm{TE}}} = \frac{4w}{\lambda\cos(\theta)}[G(p, a, \lambda, \theta) - \ln(\sin(\beta_1)] + \frac{4(2t+a)}{\lambda\cos(\theta)}[G(p, (p-w), \lambda, \theta) - \ln(\sin(\beta_2)]. \tag{4}$$

Equation (3) represents the inductance generated by the unit cell strip lines. The first term in (4) is related to the capacitance between the horizontal end dipoles spaced by a and reduced by a factor of w/p since the strips are not continuous.[41] The second term is due to the capacitance between the vertical dipole ends, which are spaced by a distance equal to $(p - w)$. For TM-incidence, X_{L1} and B_{C1} are given by[40–42]

$$X_{L1_{\mathrm{TM}}} = \frac{p}{\lambda\cos(\theta)}[G(p, t, \lambda, \theta) - \ln(\sin(\beta)], \tag{5}$$

$$B_{C1_{\mathrm{TM}}} = \frac{4w}{\lambda}\cos(\theta)[G(p, a, \lambda, \theta) - \ln(\sin(\beta_1)] + \frac{4(2t+a)}{\lambda}\cos(\theta)[G(p, (p-w), \lambda, \theta) - \ln(\sin(\beta_2)]. \tag{6}$$

The function $G(p, x, \lambda, \theta)$ and β are defined by (1), where x represents the second argument in this function as defined in (3)– (6) and $C_{1\pm}$ is the correction factor for the TE and TM

modes, respectively, given by[42]

$$C_{1\pm TE} = \frac{1}{\left[1 \pm \frac{2p\sin(\theta)}{\lambda} - \left(\frac{p\cos(\theta)}{\lambda}\right)^2\right]^{\frac{1}{2}}} - 1 \quad (7)$$

and by

$$C_{1\pm TM} = \frac{1}{\left[1 - \left(\frac{p}{\lambda}\right)^2\cos(\theta)\right]^{\frac{1}{2}}} - 1. \quad (8)$$

The transmission coefficient for the TE- and TM-incidence is given by

$$S_{21} = \frac{1}{\left(1 + \frac{0.25}{X_{L1} - \frac{1}{B_{C1}}}\right)^{\frac{1}{2}}}. \quad (9)$$

Figures 5(a) and 5(b) display the transmission coefficients for TE- and TM-incidence at different angles for the first resonance for the crosses defined with the parameters indicated. The results from the ECM have shown operation at 3 GHz and angular stability for $\theta = \{0°, 10°, 20°, 30°\}$ as well as polarization stability. These conclusions are supported by the numerical results in Figs. 5(c) and 5(d) using a full-wave analysis through the COMSOL Multiphysics software. Note that a second resonance appeared at around 4 GHz in the full-wave analysis for TE-incidence and $\theta \geq 10°$, which depends on the incident angle. Due to the model's simplicity, this resonance does not appear in the ECM. However, it has been observed from the literature's full numerical wave and experimental analysis.[40,41]

The lower frequency peak in Fig. 5 arises from the resonant behavior of individual unit cells in the metasurface. This can be confirmed from the electric near-field profile (with **E** pointing along the horizontal direction) in Fig. 6(a), where a near-field coupling between neighboring unit cells is seen. Furthermore, Figs. 5(a)–5(d) indicate that this resonance occurs under both TE and TM incident waves. In contrast, the higher frequency peak

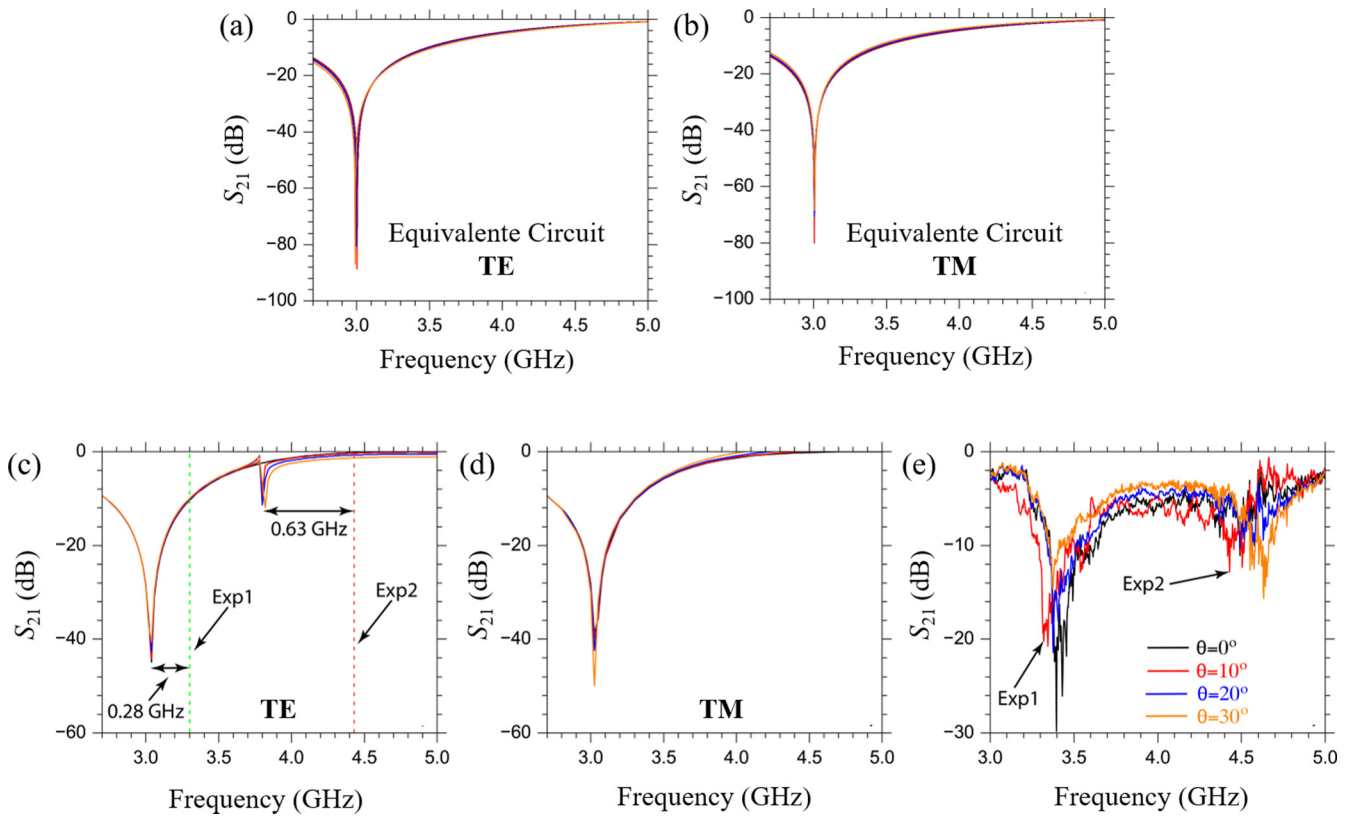

FIG. 5. Numerical results for S_{21} with the ECM for (a) TE- and (b) TM-incidence. Full-wave numerical results for the S_{21} parameter of the metasurface for (c) TE and (d) TM polarized incident waves. Experimental results for the S_{21} parameter of the metasurface for (e) TE polarized incident waves. The minimum peaks labeled Exp1 and Exp2 in (e) are used for comparative purposes in (c), where these values are represented by vertical dashed lines. The corresponding angle of incidence for each measurement is shown in (e).

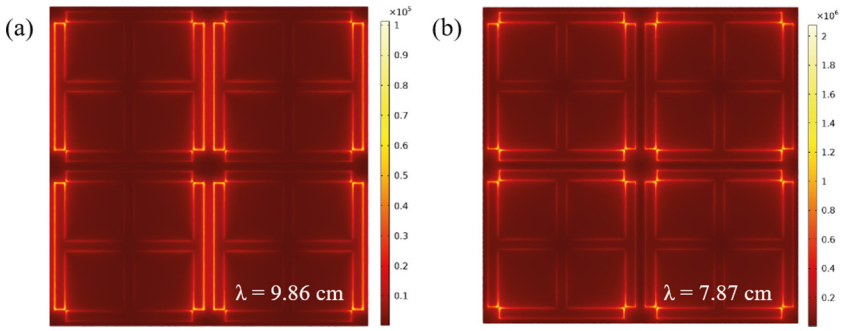

FIG. 6. Numerical results for the modulus of the electric near-field profiles ($|E|$) are shown in (a) for $f = 3.04$ GHz ($\lambda = 9.86$ cm), (b) for $f = 3.81$ GHz ($\lambda = 7.87$ cm).

only occurs for obliquely incident TE polarization. This latter observation is explained using Faraday's law: the component of the magnetic field perpendicular to the surface (under oblique TE incidence) induces a circulating current in the split square loops that lie between the corners of the adjacent unit cells, as noticed from the near-field profile in Fig. 6(b).

Since we are interested in filtering a narrow frequency range, we measured the S_{21} parameter. Experimental data are shown in Fig. 5(e) for $\theta = \{0°, 10°, 20°, 30°\}$. In contrast with the single peak behavior ($S_{21} < -10$ dB) for $\theta = 0°$, two peaks occur for $\theta \geq 10°$, consistent with the results in Fig. 5(c). For comparative purposes, we labeled Exp1 = 3.32 GHz and Exp2 = 4.44 GHz the minimum of S_{21} associated with the frequencies for the first and second experimental peaks with $\theta = 10°$, as indicated by arrows in Fig. 5(e). These latter values are compared with their simulated counterparts in Fig. 5(c). Several factors explain the differences between the experimental and numerical results, as follows: (i) numerical results are for pure TE and TM polarized fields, whereas experimental measurements (conducted in an open-field) are associated with unpolarized transverse electromagnetic (TEM) waves (see Figs. 1 and 3); (ii) simulations are for an infinite periodic 2D array of unit cells, whereas the finite size metasurface consists of an 8×8 unit cell arrangement; (iii) although the simulations for Au are the same as those for a perfect electric conductor (PEC), the parameters of the PET were used from the literature,[40] i.e., not specifically measured for the type of PET we used.

The proposed manufacturing method for telecommunications in the C-band is validated by the excellent qualitative agreement between the experimental and numerical results, despite minor discrepancies. Such small differences between calculated and measured results come from the sum of various contributions: (i) the dielectric properties of the substrate were assumed from the available literature, not directly measured for the specific PET we used (which can slightly vary according to the preparation method); (ii) though the fabricated structure is relatively large, it is not infinite, as considered in the simulation setup. Notably, the lower-frequency peak, both simulated and measured, exhibits remarkable angular and polarization robustness [see Figs. 5(a)–5(d)]. Such characteristics are suitable for band-stop electromagnetic interference shielding. For instance, non-flat surfaces can be strategically covered to redirect the wavefront toward a desired direction or serve as a conformal reflector for high-gain radiators.[33,43] The use of PET as the material of choice offers several advantages. PET possesses a melting temperature (T_m) around 250°C and demonstrates exceptional hydrolytic stability, providing flexibility and high resistance to breakage. Moreover, PET can be recycled through chemical depolymerization into its monomers or other valuable chemicals, making it an environmentally friendly option. Various ecological methods also exist for PET recycling.[44,45] In fact, PET-based antennas can be manufactured using recycled bottles.[46] Leveraging these features, the application of PET-based antennas in smart clothing becomes feasible. Such flexible materials offer user comfort while maintaining high antenna gain, thereby enabling high-performance wearable devices.[47,48]

IV. CONCLUSION

We have introduced a novel concept for manufacturing flexible screen-printed metasurfaces by combining two cost-effective and widely available techniques. The process involves utilizing a cutter printer to create screen-printed masks and employing thermal evaporation for the nanofabrication of metal thin films using the well-established thermal evaporation method. We designed the unit cell of the metasurface using electromagnetic simulation software, ensuring its optimal performance. This unit cell was printed onto a suitable substrate covered with a mask (in this case, PET was used). The resulting metasurfaces exhibit excellent qualitative agreement between numerical simulations and experimental measurements. The main resonance of the FSS is accurately explained using the equivalent-circuit model, demonstrating strong correlation with full-wave numerical simulations conducted through COMSOL Multiphysics. Our method enables the fabrication of metasurfaces from nanometric to centimeter scales, as demonstrated in this study. As a proof of concept, we have constructed an FSS consisting of an array of 8×8 unit cells operating within the frequency range of 3–5 GHz. This frequency range is essential for sub-6 GHz telecommunications bands, particularly, in the context of 5G applications. By further developing mechanisms for creating screen-printed masks, we anticipate the extension of this methodology to the manufacturing of flexible metasurfaces operating in the THz and infrared frequency ranges, which may be necessary to deploy future 6G networks.

ACKNOWLEDGMENTS

This work was partially supported by RNP, with resources from MCTIC, Grant No. 01245.020548/2021-07, under the Brazil 6G

project of the Radiocommunication Reference Center (Centro de Referência em Radiocomunicações—CRR) of the National Institute of Telecommunications (Instituto Nacional de Telecomunicações—Inatel), Brazil, and by Huawei, under the project Advanced Academic Education in Telecommunications Networks and Systems, Contract No. PPA6001BRA23032110257684. The authors also wish to acknowledge the financial support from the Brazilian agencies CAPES, FINEP, FAPEMIG, FAPESP (Nos. 2017/25587-5, 2018/22214-6, 2021/06946-0, and 2022/14229-9) and the National Council for Scientific and Technological Development-CNPq (Nos. 313036/2020-9, 311470/2021-1, 403827/2021-3, 303282/2021-5, and 314671/2021-8). E.M.M. and F.R.G acknowledge the financial support through the Senior Postdoctoral Fellowship Grant from CNPq (No. 102127/2022-0) and the Postdoctoral Fellowship from Projeto Brasil 6G Fase 2—Extensão do Projeto de Pesquisa e Desenvolvimento Tecnológico em Sistemas de Comunicações Moveis de 6ª Geração, respectively. The authors want to express their gratitude to the thin films sector group (at the IFSC-USP) for their invaluable collaboration in depositing the gold film onto PET. Particularly, they wish to express our deep appreciation to Dr. Marcos Aparecido Antonio for his substantial contribution and expertise in assisting us with this process.

AUTHOR DECLARATIONS

Conflict of Interest

The authors have no conflicts to disclose.

Authors Contributions

E. M. Materón: Conceptualization (equal); Investigation (equal); Methodology (equal). **H. R. D. Filgueiras:** Investigation (equal); Methodology (equal). **E. C. Vilas Boas:** Formal analysis (equal); Writing – original draft (equal). **F. R. Gómez:** Formal analysis (equal); Methodology (equal). **F. R. P. Cavalcanti:** Funding acquisition (equal); Resources (equal). **Y. C. B. Silva:** Funding acquisition (equal); Resources (equal). **Arismar Cerqueira S., Jr.:** Funding acquisition (equal); Resources (equal). **F. A. P. de Figueiredo:** Funding Acquisition (equal); Resources (equal). **L. L. Mendes:** Funding acquisition (equal); Resources (equal). **Osvaldo N. Oliveira Jr.:** Funding acquisition (equal); Resources (equal); Writing – review & editing (lead). **J. R. Mejía-Salazar:** Supervision (equal); Writing – original draft (equal); Writing – review & editing (equal).

DATA AVAILABILITY

The data that support the findings of this study are available from the corresponding author upon reasonable request.

REFERENCES

[1]P. Popovski, K. F. Trillingsgaard, O. Simeone, and G. Durisi, "5G wireless network slicing for eMBB, URLLC, and mMTC: A communication-theoretic view," IEEE Access **6**, 55765–55779 (2018).
[2]I. A. Alimi, R. K. Patel, N. J. Muga, A. N. Pinto, A. L. Teixeira, and P. P. Monteiro, "Towards enhanced mobile broadband communications: A tutorial on enabling technologies, design considerations, and prospects of 5G and beyond fixed wireless access networks," Appl. Sci. **11**, 10427 (2021).
[3]S. K. Sharma and X. Wang, "Toward massive machine type communications in ultra-dense cellular iot networks: Current issues and machine learning-assisted solutions," IEEE Commun. Surv. Tutor. **22**, 426–471 (2019).
[4]J. Hwang, L. Nkenyereye, N. Sung, J. Kim, and J. Song, "Iot service slicing and task offloading for edge computing," IEEE Internet Things J. **8**, 11526–11547 (2021).
[5]P. Popovski, C. Stefanović, J. J. Nielsen, E. de Carvalho, M. Angjelichinoski, K. F. Trillingsgaard, and A.-S. Bana, "Wireless access in ultra-reliable low-latency communication (URLLC)," IEEE Trans. Commun. **67**, 5783–5801 (2019).
[6]L. L. Mendes, C. S. Moreno, M. V. Marquezini, A. M. Cavalcante, P. Neuhaus, J. Seki, N. F. T. Aniceto, H. Karvonen, I. Vidal, F. Valera, P. A. S. M. Barreto, M. F. Caetano, W. D. Dias, and G. Fettweis, "Enhanced remote areas communications: The missing scenario for 5G and beyond 5G networks," IEEE Access **8**, 219859–219880 (2020).
[7]"5G NR, Base Station (BS) radio transmission and reception (3GPP TS 38.104 version 15.2.0 Release 15)," Technical Report (2018), available at https://www.etsi.org/deliver/etsi_ts/138100_138199/138104/15.02.00_60/ts_138104v150200p.pdf.
[8]E. I. Adegoke, E. Kampert, and M. D. Higgins, "Channel modeling and over-the-air signal quality at 3.5 GHz for 5G new radio," IEEE Access **9**, 11183–11193 (2021).
[9]L. Zhang, W. Nie, G. Feng, F.-C. Zheng, and S. Qin, "Uplink performance improvement by decoupling uplink/downlink access in HetNets," IEEE Trans. Veh. **66**, 6862–6876 (2017).
[10]M. A. Lema, E. Pardo, O. Galinina, S. Andreev, and M. Dohler, "Flexible dual-connectivity spectrum aggregation for decoupled uplink and downlink access in 5G heterogeneous systems," IEEE J. Sel. Areas Commun. **34**, 2851–2865 (2016).
[11]P. Zhang, B. Yang, C. Yi, H. Wang, and X. You, "Measurement-based 5G millimeter-wave propagation characterization in vegetated suburban macrocell environments," IEEE Trans. Antennas Propag. **68**, 5556–5567 (2020).
[12]E. C. Vilas Boas, F. A. de Figueiredo, L. L. Mendes, and R. A. de Souza, "Artificial intelligence for channel estimation in multicarrier systems for B5G/6G communications: A survey," EURASIP J. Wirel. Commun. Netw. **2022**, 1–63 (2022).
[13]C. Sacchi, T. F. Rahman, I. A. Hemadeh, and M. El-Hajjar, "Millimeter-wave transmission for small-cell backhaul in dense urban environment: A solution based on MIMO-OFDM and space-time shift keying (STSK)," IEEE Access **5**, 4000–4017 (2017).
[14]H. Zhang, Y. Cheng, and F. Chen, "Quad-band plasmonic perfect absorber using all-metal nanostructure metasurface for refractive index sensing," Optik **229**, 166300 (2021).
[15]Y. Cheng and J. Zhao, "Simple design of a six-band terahertz perfect metasurface absorber based on a single resonator structure," Phys. Scr. **97**, 095508 (2022).
[16]L. Li, T. Jun Cui, W. Ji, S. Liu, J. Ding, X. Wan, Y. Bo Li, M. Jiang, C.-W. Qiu, and S. Zhang, "Electromagnetic reprogrammable coding-metasurface holograms," Nat. Commun. **8**, 197 (2017).
[17]W.-L. Song, Z. Zhou, L.-C. Wang, X.-D. Cheng, M. Chen, R. He, H. Chen, Y. Yang, and D. Fang, "Constructing repairable meta-structures of ultra-broad-band electromagnetic absorption from three-dimensional printed patterned shells," ACS Appl. Mater. Interfaces **9**, 43179–43187 (2017).
[18]L. Chen, H. L. Ma, and H. Y. Cui, "Wavefront manipulation based on mechanically reconfigurable coding metasurface," J. Appl. Phys. **124**, 043101 (2018).
[19]L. Chen, H. L. Ma, Y. Ruan, and H. Y. Cui, "Dual-manipulation on wave-front based on reconfigurable water-based metasurface integrated with pin diodes," J. Appl. Phys. **125**, 023107 (2019).
[20]Y. Saifullah, Q. Chen, G.-M. Yang, A. B. Waqas, and F. Xu, "Dual-band multi-bit programmable reflective metasurface unit cell: Design and experiment," Opt. Express **29**, 2658–2668 (2021).
[21]W. Chen, J. Zhan, Y. Zhou, R. Chen, Y. Wang, and Y. Ma, "Microwave metamaterial absorbers with controllable luminescence features," ACS Appl. Mater. Interfaces **13**, 54497–54502 (2021).
[22]D. Rotshild, E. Rahamim, and A. Abramovich, "Innovative reconfigurable metasurface 2-D beam-steerable reflector for 5G wireless communication," Electronics **9**, 1191 (2020).

[23]T. Hongnara, Y. Shirasawa, T. Sasaki, K. Sasaki, K. Sato, I. Oshima, N. Michishita, H. Nakabayashi, and A. K. Cho, "Dual-polarized broad-beam reflective metasurface based on multi-sheet configuration for local 5G application at 28.25 GHz," in *2021 15th European Conference on Antennas and Propagation (EuCAP)* (IEEE, 2021), pp. 1–4.
[24]R. Ebrahimzadeh, B. Zakeri, A. Darvish, and S. E. Hosseininejad, "Multi beam scanning programmable metasurface using miniaturized unit cells for 5G applications," J. Electromagn. Waves Appl. **15**, 2164–2177 (2022).
[25]N. Shlezinger, G. C. Alexandropoulos, M. F. Imani, Y. C. Eldar, and D. R. Smith, "Dynamic metasurface antennas for 6G extreme massive MIMO communications," IEEE Wirel. Commun. **28**, 106–113 (2021).
[26]F. Yang, P. Pitchappa, and N. Wang, "Terahertz reconfigurable intelligent surfaces (RISs) for 6G communication links," Micromachines **13**, 285 (2022).
[27]M. Najafi and R. Schober, "Intelligent reflecting surfaces for free space optical communications," in *2019 IEEE Global Communications Conference (GLOBECOM)* (IEEE, 2019), pp. 1–7.
[28]L. Zhan, H. Zhao, W. Zhang, and J. Lin, "An optimal scheme for the number of mirrors in vehicular visible light communication via mirror array-based intelligent reflecting surfaces," Photonics **9**, 129 (2022).
[29]R. S. Anwar, L. Mao, and H. Ning, "Frequency selective surfaces: A review," Appl. Sci. **8**, 1689 (2018).
[30]S. S. Bukhari, J. Vardaxoglou, and W. Whittow, "A metasurfaces review: Definitions and applications," Appl. Sci. **9**, 2727 (2019).
[31]H.-X. Xu, S. Tang, S. Ma, W. Luo, T. Cai, S. Sun, Q. He, and L. Zhou, "Tunable microwave metasurfaces for high-performance operations: Dispersion compensation and dynamical switch," Sci. Rep. **6**, 38255 (2016).
[32]O. P. Falade, S. F. Jilani, A. Y. Ahmed, T. Wildsmith, P. Reip, K. Z. Rajab, and A. Alomainy, "Design and characterisation of a screen-printed millimetre-wave flexible metasurface using copper ink for communication applications," Flex. Print. Electron. **3**, 045005 (2018).
[33]H. Matsui, M. Shoji, S. Higano, H. Yoda, Y. Ono, J. Yang, T. Misumi, and A. Fujita, "Infrared plasmonic metamaterials based on transparent nanoparticle films of In_2O_3:Sn for solar-thermal shielding applications," ACS Appl. Mater. Interfaces **14**, 49313–49325 (2022).
[34]J. Zhu, Z. Hu, S. Zhang, X. Zhang, H. Zhou, C. Xing, H. Guo, D. Qiu, H. Yang, C. Song, and H. Cheng, "Stretchable 3D wideband dipole antennas from mechanical assembly for on-body communication," ACS Appl. Mater. Interfaces **14**, 12855–12862 (2022).
[35]J. Zhang, L. Shao, Z. Li, C. Zhang, and W. Zhu, "Graphene-based optically transparent metasurface capable of dual-polarized modulation for electromagnetic stealth," ACS Appl. Mater. Interfaces **14**, 31075–31084 (2022).
[36]G. Tomaszewski, P. Jankowski-Mihułowicz, J. Potencki, A. Pietrikova, and P. Lukacs, "Inkjet-printed HF antenna made on PET substrate," Microelectron. Reliab. **129**, 114473 (2022).
[37]Y. Yoo, H. Jeong, D. Lim, and S. Lim, "Stretchable screen-printed metasurfaces for wireless strain sensing applications," Extreme Mech. Lett. **41**, 100998 (2020).
[38]R. Carvalho, R. Brito-Pereira, N. Pereira, A. C. Lima, C. Ribeiro, V. Correia, S. Lanceros-Mendez, and P. Martins, "Improving the performance of paper-based dipole antennas by electromagnetic flux concentration," ACS Appl. Mater. Interfaces **15**, 11234–11243 (2023).
[39]A. L. Kamyshny, J. H. G. Steinke, and S. Magdassi, "Metal-based inkjet inks for printed electronics," Open Appl. Phys. J. **4**, 19–36 (2011).
[40]L. B. Wang, K. Y. See, J. W. Zhang, B. Salam, and A. C. W. Lu, "Ultrathin and flexible screen-printed metasurfaces for EMI shielding applications," IEEE Trans. Electromagn. Compat. **53**, 700–705 (2011).
[41]R. Langley and A. Drinkwater, "Improved empirical model for the Jerusalem cross," in *IEE Proceedings H (Microwaves, Optics and Antennas)* (IET, 1982), Vol. 129, pp. 1–6.
[42]C. K. Lee and R. Langley, "Equivalent-circuit models for frequency-selective surfaces at oblique angles of incidence," in *IEE Proceedings H (Microwaves, Optics and Antennas)* (IET, 1985), Vol. 132, pp. 395–399.
[43]H. Li, C. Ma, F. Shen, K. Xu, D. Ye, J. Huangfu, C. Li, L. Ran, and T. A. Denidni, "Wide-angle beam steering based on an active conformal metasurface lens," IEEE Access **7**, 185264–185272 (2019).
[44]S. Mandal and A. Dey, "PET chemistry," in *Recycling of Polyethylene Terephthalate Bottles, Plastics Design Library*, edited by S. Thomas, A. Rane, K. Kanny, A. V.K., and M. G. Thomas (William Andrew Publishing, 2019), Chap. 1, pp. 1–22.
[45]C. J. Chirayil, R. K. Mishra, and S. Thomas, "Materials recovery, direct reuse and incineration of PET bottles," in *Recycling of Polyethylene Terephthalate Bottles, Plastics Design Library*, edited by S. Thomas, A. Rane, K. Kanny, A. V. K., and M. G. Thomas (William Andrew Publishing, 2019), Chap. 3, pp. 37–60.
[46]J. R. Camargo, T. A. Silva, G. A. Rivas, and B. C. Janegitz, "Novel eco-friendly water-based conductive ink for the preparation of disposable screen-printed electrodes for sensing and biosensing applications," Electrochim. Acta **409**, 139968 (2022).
[47]T. Govindan, S. K. Palaniswamy, M. Kanagasabai, S. Kumar, M. Marey, and H. Mostafa, "Design and analysis of a flexible smart apparel MIMO antenna for bio-healthcare applications," Micromachines **13**, 1919 (2022).
[48]Z. Deng, L. Guo, X. Chen, and W. Wu, "Smart wearable systems for health monitoring," Sensors **23**, 2479 (2023).